Subproject B1.4

Preparation and Characterization of Metallic Nanostructures

Principle Investigators: Hilbert v. Löhneysen, Christoph Sürgers, Regina Hoffmann

CFN-Financed Scientists: Timofey Balashov (1/2 BAT IIa, 3 months), B. Gopalakrishnan (3/4 BAT IIa, 6 months), Daniel Kaufmann (1/2 BAT IIa, 2 months), Markus Sauter (3/4 BAT IIa, 16 months), Richard Montbrun (38,6% BAT IIa, 44 months), Marc Müller (1/2 BAT IIa, 24 months)

Further Scientists: Dominik Stöffler, Gerda Fischer

Physikalisches Institut
KIT – Campus Süd

B1.4 v. Löhneysen, Sürgers, Hoffmann

Preparation and Characterization of Metallic Nanostructures

Introduction and Summary

In this subproject, metallic nanostructures approaching the atomic scale are prepared by various techniques employing "top-down" methods like electron-beam lithography, mechanically controlled break junctions, and nanostructured point contacts through free-standing membranes, as well as "bottom-up" methods like self-organized metallic structures on single-crystalline surfaces. A general focus of subproject B1.4 is to explore the intimate relation between structures and defects in metallic nanostructures on the one hand, and their electronic properties on the other hand. Metallic nanostructures prepared in the present project are needed for the investigation of electronic transport properties at low temperatures and in magnetic fields focussing on hybrid nanostructures, see B2.7.

The Si(557):Au surface is of prime interest as "self-organized" quasi one-dimensional metallic structure. An issue of considerable debate is a possible Peierls instability of the Au chains forming on terraces of vicinal Si(111) for appropriate Au coverage. We have identified strong structural correlations between defects at step edges and Si-adatom chains on the same terrace, with little correlation to the closer (!) Si-adatom chain on the lower terrace. These findings – together with *T*-dependent measurements – speak agains a Peierls instability. Structural aspects leading to strong implications for electronic properties were also investigated for Ag nanoislands on Nb(110). We found a surprisingly strong shift of the electronic surface-state energy in the Γ-L bandgap with the Nb-induced mechanical in-plane strain. Continuous "tuning" of the surface-state energy is accomplished by investigating wedge-shaped islands exploiting the thickness-dependent relaxations of the Nb-induced strain.

While in our previous work we have employed mechanically controlled break junctions to investigate a number of electronic properties down to the level of single atoms and molecules, the route to alternative control parameters of an electrode gap of 1-nm size and below has been difficult. We have succeeded in realizing magnetostrictive break junctions with wires of Dy which has a very large magnetostrictive constant. Not only were we able to induce magnetic field switching between on and off states of a Dy contact, but also observed conductance plateaux and conductance jumps from which conductance histograms were obtained. The directional dependence of switching of the wire with respect to the field direction was determined for single-crystalline Dy wire and was found to be in accord with the behavior expected from magnetization measurements.

Dilute magnetic semiconductors have been proposed as materials for spintronic devices. However, the issue of transition-metal precipitates leading to superparamagnetism instead of ferromagnetism has been a recurring issue. We therefore, in collaboration with project A2.7, magnetically characterized epitaxial GaN:Cu films that have the advantage that possible metallic Cu precipitates are nonmagnetic. For GaN with 1.2 at% Cu, we find a stable ferromagnetic hysteresis loop at 10 K that persists up to 290 K with no noticeable decrease of the saturation magnetization. A ferromagnetic signal could be traced up to 400 K, the highest measuring temperature. Another promising material for implementation into semiconductor-based magnetoelectronic devices is ferromagnetic carbon-doped Mn_5Si_3C. We have successfully demonstrated that the initially carbon-free Mn_5Si_3 can be patterend by C^+-ion implantation through a mechanical mask to obtain a magnetic hybrid structure of ferromagnetic Mn_5Si_3C embedded in antiferromagnetic Mn_5Si_3.

To contact metallic nanostructures for electronic transport measurements, often a lift-off technique involving organic solvents is employed. However, for the investigation of the structure of nanocontacts with an STM, solvent residues have to be avoided. We have therefore developed miniature masks for characterization and in-situ transport measurements for nanostructures of submicrometer dimensions under UHV conditions. Finally, we have used controlled electromigration to fabricate nanocontacts by defining a thinning process of a mteallic wire that limits the power dissipated during intermittant electromigration pulses rather than the voltage.

1. Structural Correlations Between One-Dimensional Structures at the Si(557)-Au Surface

Among the one-dimensional (1D) reconstructions induced by submonolayer-thin metals on single-crystalline semiconductor surfaces, the Si(557):Au surface has attracted considerable interest due to its unusual electronic properties found by angular resolved photoelectron spectroscopy (ARPES) [1,2]. A shift of the position of the upper band from E_F at room temperature (RT) to 40 meV below E_F at 77 K was interpreted as a Peierls-like instability with a mean-field transition temperature T_c = 260 K [2]. A Peierls transition can only occur at finite temperatures in the presence of (albeit weak) additional correlations between the 1D structures. In search of such correlations on an atomic scale we have re-examined the Si(557):Au surface by STM with high lateral and vertical (height) resolutions at T = 300 and 77 K [B1.4:2,B1.4:3].

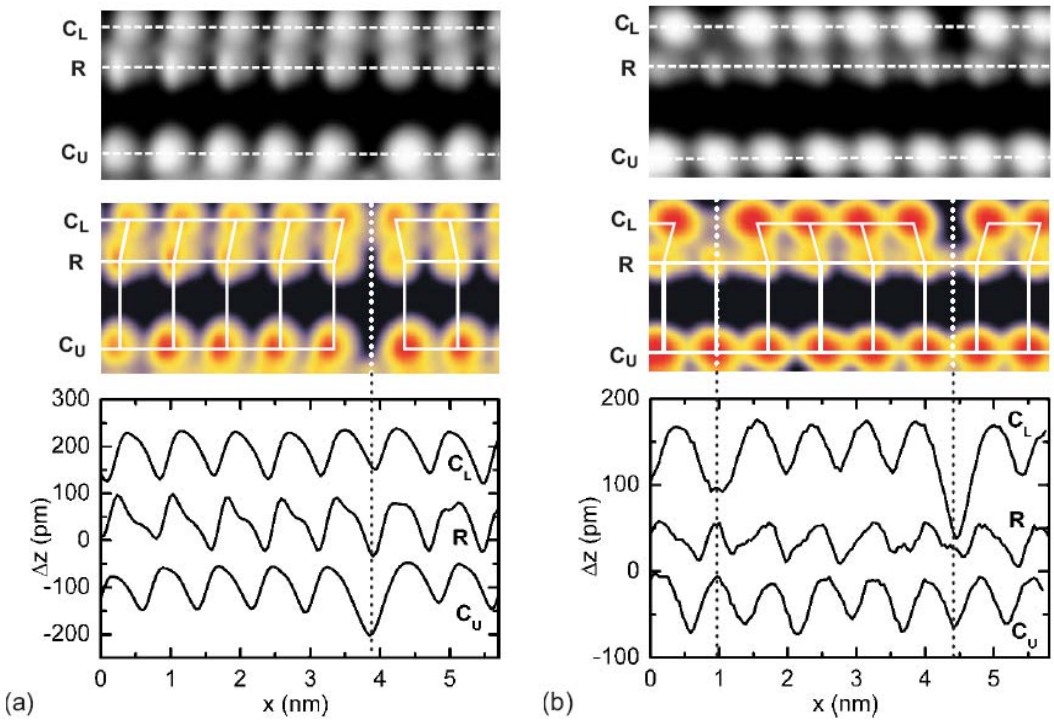

Fig. 1: (a) STM image (T = 77 K, U = +1 V, and I = 0.05 nA; top) showing a step edge R and the adjacent adatom chains located on the lower (C_L) and upper (C_U) terraces containing a defect on R and C_U. Horizontal dashed lines indicate traces of the height profile scans $\Delta z(x)$ (bottom). White lines (middle) indicate the correlation between atoms on C_U and the upper atoms of the buckled step edge (R). Vertical dotted lines indicate a local mirror symmetry between the two configurations. (b) STM image (T = 77 K, U = +1 V, and I = 0.1 nA; top) showing a step edge R and the adjacent adatom chains C_U and C_L with two phase-shifting defects on C_L. From Ref. [B1.4:3].

In our STM images we denote the monoatomic structures as C for "chain" of localized protrusions and R for "row". Figure 1(a) (top panel) shows an STM image at 77 K with two adjacent chains C belonging to the upper (C_U) and lower (C_L) of two terraces. C_U shows a defect that appears as a topographic minimum and causes a phase shift of the Si adatoms composing the chain with respect to the Si substrate. Away from the defect, the height profile taken along R has the same period as the profile along C_L and C_U, but each maximum on R shows an additional soft shoulder due to the two adjacent elliptical features of alternating heights observed on R in the STM image. This height modulation is attributed to the static buckling of the Si step edge with an almost fully occupied "up" atom and an almost unoccupied "down" atom as proposed in the first-principles calculation [3]. The phase relationship between C_U and R as well as between R and C_L is indicated by solid white lines. On both sides of the defect, this phase relationship is in agreement with the structure model either in its original or in its mirror-reflected form. The defect-induced phase shift on C_U of the upper terrace affects the periodic arrangement at R located 3 2/3 Si rows away such that a phase shift is observed at R, too. Hence, the structural correlation between adatoms on C_U and the atoms of the descending step edge (R) of the *same* terrace is maintained even in the presence of the defect.

The chain C_L on the adjacent lower terrace, on the other hand, is not affected, i.e., no phase shift is observed. This gives rise to a local mirror symmetry of the structure on terrace U that extends to C_L, cf. vertical dotted lines in Fig. 1. In contrast, the periodic arrangement of protrusions on R is not affected when a phase-shifting defect is located on C_L, i.e., on the *next* terrace. This is shown in Fig. 1(b), where two phase-shifting defects are observed on C_L. In contrast to Fig. 1(a), the periodic arrangement on R is maintained and follows the undisturbed arrangement on C_U due to the strong correlation between C_U and R. Hence, we do not observe a correlation between R and C_L located on two adjacent terraces. The correlation between R and C_U supports the proposed structure model [3] which suggests that R and C_U are located on the same terrace, in contrast to a proposal of two adjacent rows comprised of Si and Au atoms, respectively [4].

Within the structure model proposed by Sánchez-Portal et al. [3], the cutting-off of the correlations is naturally attributed to the step edge. More importantly, the observed correlation points to the presence of a strong interaction between chains C and rows R. The correlation is stronger between C_U and R separated by 3 2/3 Si nearest-neighbor (nn) distances compared to C_L and R separated by only two Si nn distances. Hence, possible correlations between the 1D structures located on different terraces are apparently disturbed by the presence of the step edge. A coupling between 1D structures is a necessary — but not a sufficient — condition for a Peierls transition at finite temperature. We have shown that structural correlations between the monoatomic chains on the Si(557):Au surface are restricted to one atomic terrace. Apart from the decisive role of the step edge, our results are largely independent of the applied structure model. Therefore, step-edge induced disruptions should be taken into account when proposing alternative models for the Si(557):Au surface.

2. Distribution of Mechanical Strain in Ag Islands of Nb (110)

We investigate the growth of Ag on Nb (110) by in-situ STM (T = 4 K) under UHV conditions. Detailed investigations concerning the growth of these metals are not available up to now. The surface of a Nb (110)-oriented single crystal is prepared by repeated cycles of high-temperature annealing ("flashing") and Ar^+ sputtering. At a substrate temperature T_S = 573 K, evaporation of nominal 5 nm Ag on Nb (110) leads to the formation of large, flat, and well separated islands (Fig. 2, inset). On top of these islands the electronic surface state in the Γ-L bandgap is resolved by local

tunnelling spectroscopy (Fig. 2, left). This state is shifted by 70 – 100 meV towards the unoccupied band when compared to the homoepitaxy of Ag on Ag (111) [5]. Previous work has shown that the shift is due to mechanical strain [6], where tensile strain of Ag(111) shifts the band edges upward. Adopting this interpretation we are able to generate a map of the local mechanical strains of Ag islands on the nanometer scale. The *dI/dV* ($V = 0$) map in Fig. 2 (right) shows a dark blue area of low conductivity separated from a yellow/red area of high conductivity. The contour of the dark blue area is the contour for which the position of the surface state band edge is at $V = 0$, i.e., at the Fermi level. The implies a shift of the band edge by 70 meV upward from which we infer an in-plane tensile strain of 0.5 % [6]. This strain is presumably not due to the epitaxial misfit of ~ 4% (average) at the interface between bcc-Nb (110) and fcc-Ag (111), which is already relieved in these thick islands. It is more likely that a thermal strain arises from the different thermal expansion coefficients α of Ag ($\alpha = 18.9\ 10^{-6}\ K^{-1}$) and Nb ($\alpha = 7.3\ 10^{-6}\ K^{-1}$) after cooling from $T_S = 573$ K to 4 K . Indeed, from the difference of α we estimate a thermal strain $\varepsilon = \Delta\alpha\ \Delta T = 0.2$ % in good agreement with a strain of 0.4 % that is needed to shift the surface state to the Fermi level [6]. From several *dI/dV* maps created for different bias voltages *V* we will be able to generate a map of local strains for Ag islands on the nanoscale. In particular, we will investigate the strain distribution of single and coalesced nanoscale islands.

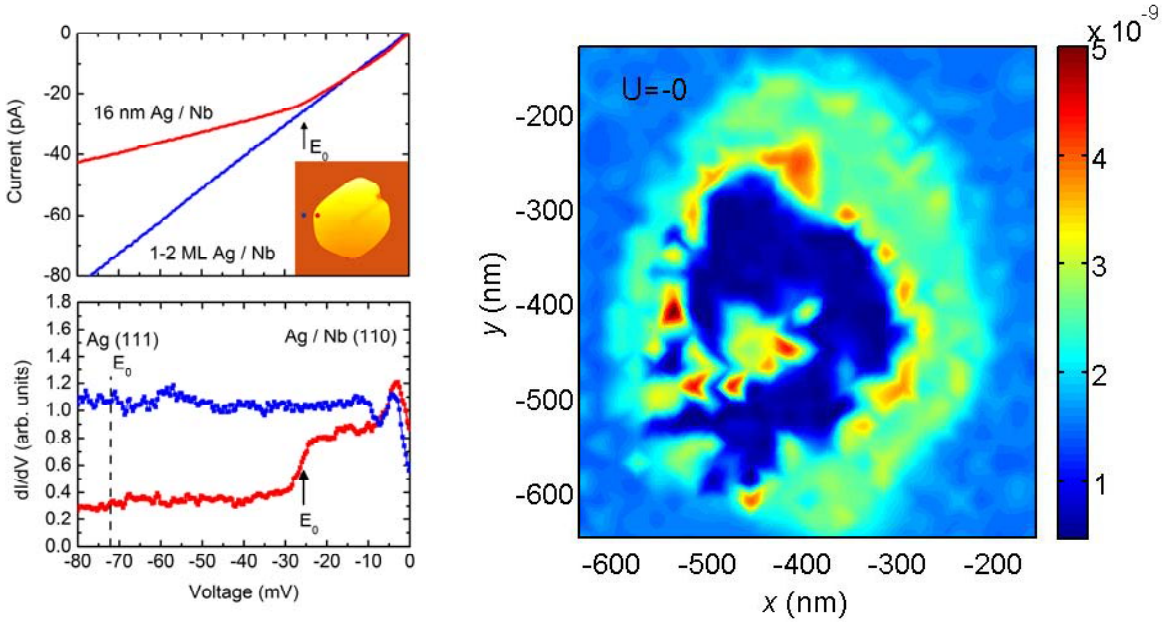

Fig. 2: Left: Tunneling current $I(V)$ (top) and differential conductance *dI/dV* (bottom) vs. bias voltage acquired over a 1 – 2 monolayer thin Ag island (blue) and over a 16 nm thick Ag island (red) on Nb (110). Arrow indicates the energy E_0 of the lower band edge of the electronic surface state in the Γ-L bandgap, dashed line shows the position of E_0 expected for bulk Ag (111). Right: *dI/dV* map of an Ag island for $V = 0$.

3. Magnetostrictive Dy Break Junctions

We exploit the large magnetostriction (MS) of the rare-earth metal dysprosium to tune the conductance *G* of a break junction by a magnetic field [B1.4:18]. Below the Curie temperature T_C = 87 K, Dy has a huge MS $\lambda = 0.003 – 0.008$. Figure 3(a) shows the field-induced switching for a polycrystalline wire in magnetic field oriented parallel to the long wire axis ($\alpha = 0$) which occurs

rather abruptly. The switching exhibits considerable hysteresis, with a width $\mu_0 \Delta H \approx 20$ mT. The change of the conductance from $G_0 \approx 0$ to high conductance with increasing field is due to the positive MS of Dy which leads to an elongation of the two electrodes and closure of the contact. In addition to field-induced complete switching between "open" and "closed" states, a step-like behavior of the conductance $G(H)$ with more or less well-defined conductance plateaux can be observed [Fig. 3(b)], resembling the behavior of mechanically controlled nanocontacts [7].

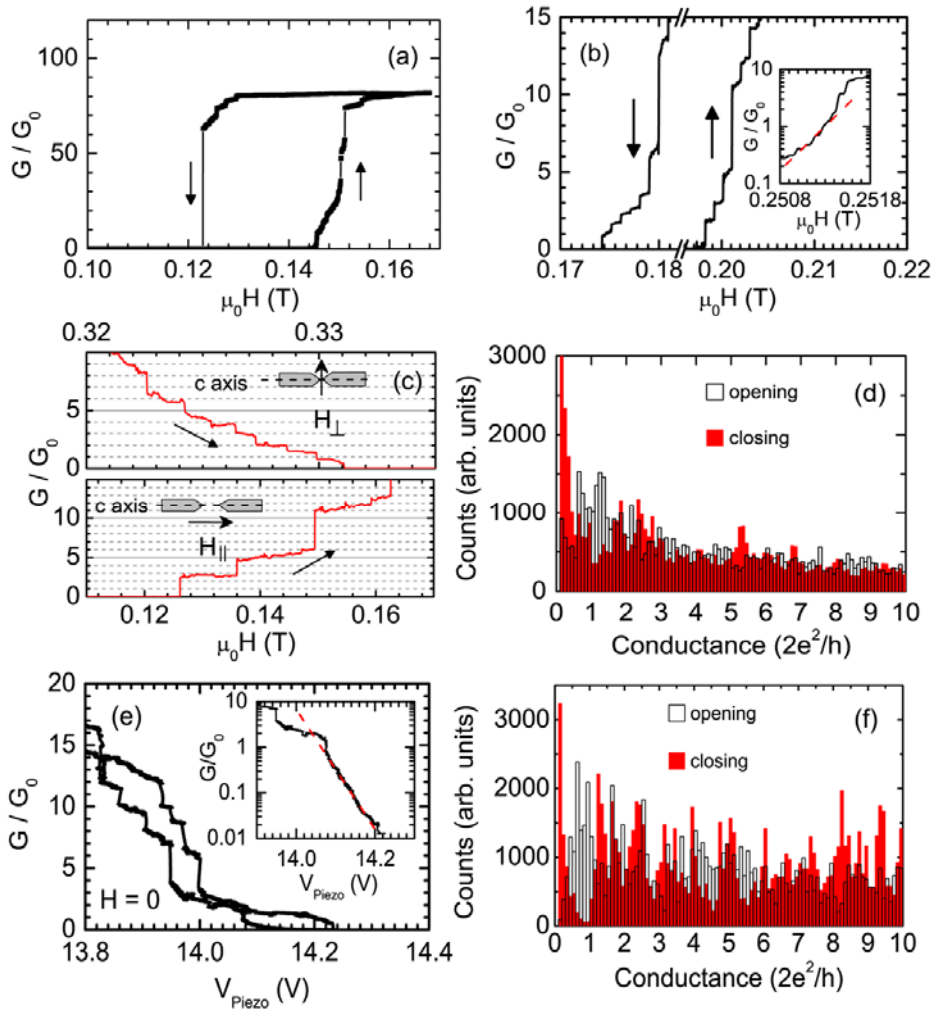

Fig. 3: (a) Conductance G vs. magnetic field H for a polycrystalline Dy wire. (b) $G(H)$ with discrete steps of G. Inset shows $G(H)$ in a semilogarithmic plot while closing the contact with increasing H. Red dashed line indicates the exponential increase of G in the tunneling regime. (c) $G(H)$ of a single-crystalline Dy wire with the c-axis oriented along the long wire axis and for H applied parallel or perpendicularly to the long wire axis. (d) Conductance histograms of all samples for opening (white bars) and closing (red bars) the contact by a magnetic field. (e) Conductance of a mechanically broken Dy wire vs. piezo voltage, i.e., electrode distance, in zero magnetic field. Inset shows $G(V_{piezo})$ in a semilogarithmic plot while closing the contact mechanically. Red dashed line indicates the exponential increase of G with decreasing V in the tunneling regime. (f) Conductance histograms of all samples for opening (white bars) and closing (red bars) the contact mechanically. From Ref. [B1.4:18]

Figure 3(c) shows *G(H)* curves measured on a single-crystalline Dy wire with the c-axis oriented parallel to the long wire axis and *H* applied parallel or perpendicularly to the long wire axis. The different behavior for parallel and perpendicular magnetic field is due to the anisotropy of the volume-invariant Joule MS.

From all the data recorded on various samples, we determined separate histograms of the conductance values *G*(*H*) for opening and closing the contact, see Fig. 3(d). The difference between these two histograms is due to a different different type of mechanical deformation of the contact for opening and closing. While opening the contact the wire is deformed plastically until a one-atom contact is established giving rise to a conductance of the order of 1 G_0. Eventually, the contact breaks with a sudden relaxation of both electrodes and an immediate increase of their distance. Subsequent closing of the contact will first lead to a tunneling current before a contact is formed. Indeed, the *G*(*H*) data during closing can be described by an exponential dependence expected for electron tunneling, see inset Fig. 3(b). Fig. 3(e) shows the mechanical switching of a polycrystalline Dy wire in zero field exhibiting the typical conductance steps of the order of G_0 found for many metallic nanocontacts. The inset shows the tunneling regime during closing. The histograms obtained for mechanically controlled break-junctions shown in Fig. 3(f) are qualitatively similar to histograms obtained for field switching, cf. Fig. 3(d). Comparison of the field- and mechanically-tuned conductance behavior yields a magnetostriction λ in good agreement with the bulk value.

We also investigated the effect of the MS anisotropy in detail by measuring the angular dependence of the conductance curves *G*(*H*) of poly- and single-crystalline samples (not shown). We conclude that the anisotropic behavior of *G*(*H*) is in full agreement with the magnetic anisotropy of the magnetization *M(H)* (not shown) and λ*(H)* which confirms that the observed behavior of a field-induced switching of the ferromagnetic nanocontact is caused by magnetostriction.

4. Magnetic Properties of Cu-Doped GaN

Dilute magnetic semiconductors (DMS) are proposed to show ferromagnetism at room-temperature and have raised interest due to their possible applications in spintronic devices. Investigations on the ferromagnetism in DMS usually focus on the doping with transition metals. Semiconducting group-III nitrides are attractive for optoelectronic applications and devices due to their large bandgap and their thermal and chemical stability. The best characterized compound among the group-III nitrides is GaN. To avoid problems with ferromagnetic transition-metal precipitates known for Mn- and Gd-doped GaN, nonmagnetic dopants such as Cu are favored. In theory, Cu-doped GaN has been discussed controversially [8,9]. Room-temperature ferromagnetism was observed for Cu^+-ion implanted GaN [10] with a much smaller magnetic moment μ= 0.01–0.27 μ_B, than predicted [8]. However, the value of μ depends sensitively on the annealing conditions possibly due to defects introduced by the ion implantation. For future applications, epitaxial growth of Cu-doped GaN would be indispensible.

In collaboration with the group of D. Schaadt (project A2.7) we study the magnetic properties of Cu-doped GaN grown by plasma-assisted molecular beam epitaxy on *C*-plane sapphire substrates. The samples are prepared and characterized structurally and chemically in project A2.7. First results have been published [B1.4:17]. The room-temperature ferromagnetism of Cu-doped GaN was explored by SQUID magnetometry between 10 K and 400 K with the magnetic field applied parallel to the film plane. For sample N121, a ferromagnetic signal with small coercivity is observed even at room-temperature (Fig. 4). For comparison, the nonmagnetic behaviour of undoped GaN is also shown. For this sample, the magnetic saturation corresponds to a magnetic moment of 0.58 μ_B

per Cu atom. This is lower than 2.0 μ_B predicted by Wu et al. [8]. However, the true Cu concentration in the GaN film maybe lower than 1.2 % due to the formation of Cu-Ga islands at the surface. Hence, the moment per Cu atom incorporated in GaN may be much larger. An important issue for possible spintronic applications is the Curie temperature T_C. The MBE-grown Cu-doped GaN shows ferromagnetic behavior even at 400 K (not shown). To exclude that the Cu-Ga islands on the surface cause the ferromagnetic behavior, we intentionally deposited Cu-Ga alloys on top of pure GaN at a low temperature. This sample showed diamagnetic behavior. Therefore, the observed ferromagnetic behavior must be caused by Cu incorporation into the GaN lattice. The origin of ferromagnetic behavior in Cu-doped GaN is still unclear. On the one hand, Cu could be incorporated in the GaN lattice on Ga sites inducing ferromagnetic behavior by Zener double exchange or p-d hybridization [8]. On the other hand, the incorporation of Cu may cause magnetically active lattice defects, such as point defects, interstials, voids, dangling bonds etc., which could be an origin of the ferromagnetic behavior [11]. This will be investigated further.

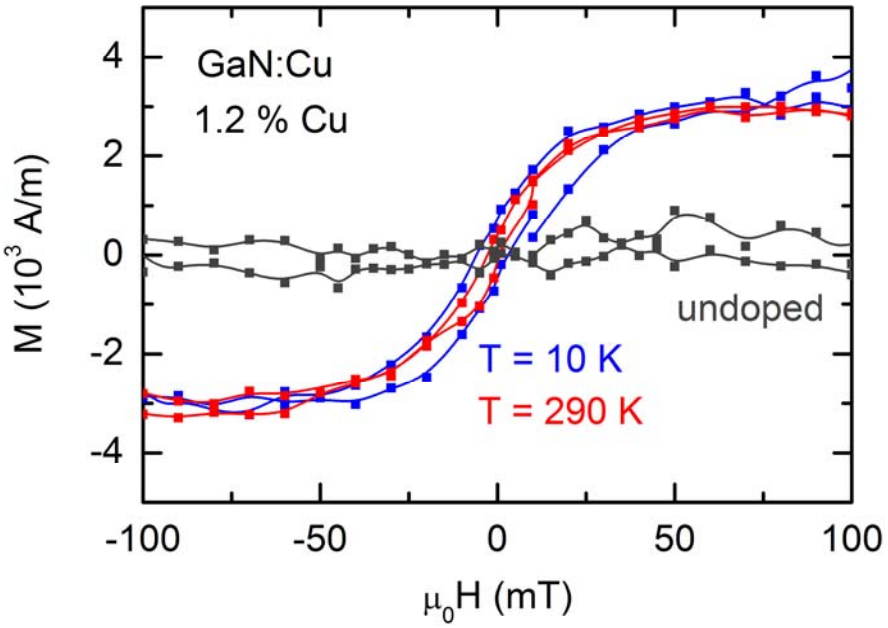

Fig. 4: Magnetization M vs magnetic field H of undoped GaN and of 1.2% Cu-doped GaN measured at 10 K and at 290 K.

5. Lateral Modification of Magnetic Order by C-Ion Implantation

Metal-semiconductor compounds such as Mn_5Ge_3 have been considered as promising candidates due to their easy implementation into the semiconductor-based device fabrication technology [12] The rather low Curie temperature T_C = 304 K of Mn_5Ge_3 is a severe disadvantage for technological applications. However, the isostructural antiferromagnetic Mn_5Si_3 (T_N = 99 K) can be driven ferromagnetic by insertion of carbon yielding $Mn_5Si_3C_{0.8}$ with T_C = 350 K [13]. Hence, ferromagnetic $Mn_5Si_3C_x$ could be an appealing material for implementation into semiconductor-based magnetoelectronic devices. In an alternative approach to cosputtering of Mn, Si or Ge, and C, we investigated ferromagnetic $Mn_5Si_3C_{0.8}$ films prepared by implantation of carbon ions into antiferromagnetic Mn_5Si_3 [B1.4:9]. Each 400-nm-thick Mn_5Si_3 film was prepared by magnetron sputtering as described earlier [13] and was protected by 5–10 nm Si or Ge to avoid oxidation in air during transfer to the ion implanter. $^{12}C^+$-ion implantation was performed in three steps of 195, 100,

and 45 keV energy. The respective ion doses were chosen to yield $Mn_5Si_3C_{0.8}$. The structure of all polycrystalline films was of Mn_5Si_3 type (hexagonal $D8_8$ structure) as checked by θ-2θ x-ray diffractometry. The temperature dependent resistivity of C-implanted films shows metallic behavior. The implanted $Mn_5Si_3C_{0.8}$ film had the same Curie temperature T_C = 350 K as the sputtered film. In addition, the implanted film showed a reduced coercivity and a higher saturation moment m_S = 1.2 μ_B/Mn than the sputtered film. This is the highest moment for ferromagnetic $Mn_5Si_3C_{0.8}$ reported so far.

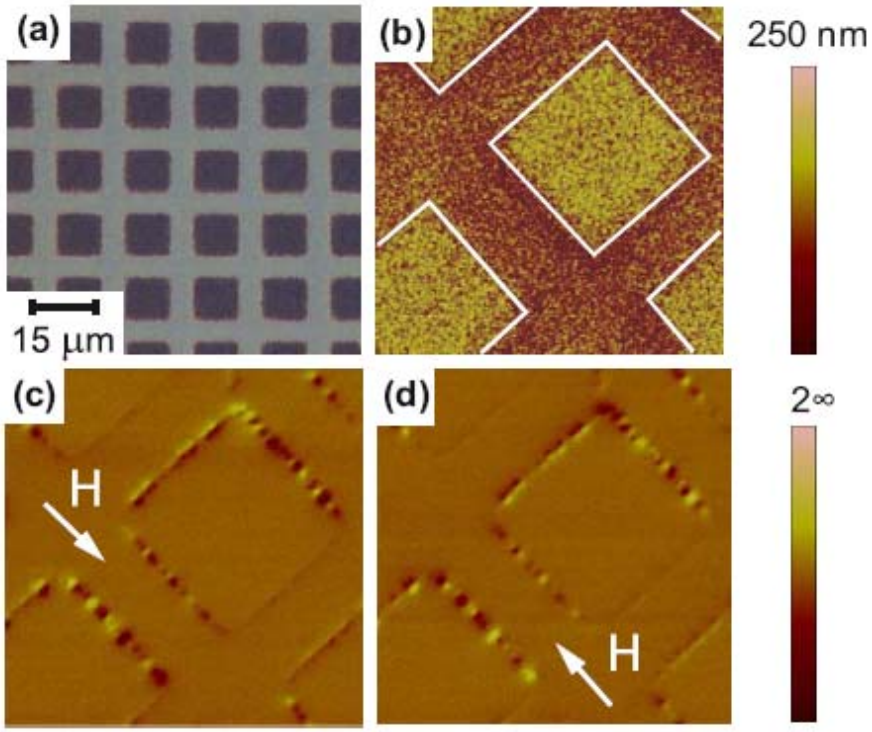

Fig. 5: (a) Optical micrograph of Mn_5Si_3 irradiated with $12C^+$ ions through a 7 x 7 μm^2 gold mesh. C-implanted regions appear dark. (b) AFM image (25 x 25 μm^2) of the topography. Ion-irradiated squares are indicated by white lines. (c) MFM images taken in an applied magnetic field $\mu_0 H$ = 50 mT and (d) after field reversal. From Ref. [B1.4:9]

We focused on the lateral modification of the magnetic order of C-implanted $Mn_5Si_3C_{0.8}$ by ion implantation. Patterning was achieved by using a commercially available 100-μm-thick gold mesh with 7 x 7 μm^2 square openings serving as a stencil mask during implantation of a virgin carbon-free film. Figure 5(a) shows an optical micrograph and Fig. 5(b) an AFM image of patterned $Mn_5Si_3/Mn_5Si_3C_{0.8}$, both taken at room temperature. The implanted areas show an implantation-induced expansion perpendicular to the surface (swelling). This is attributed to the ion-induced formation of voids in the film at T_S = 450 °C.

For patterned $Mn_5Si_3/Mn_5Si_3C_{0.8}$ no magnetic contrast was observed in MFM images taken in the remanent state at zero applied field (not shown). Figures 5(c) and (d) show MFM images taken in a field of $\mu_0 H$ = 50 mT applied in the plane along the directions indicated. A magnetic contrast is only observed for micrometer-sized circular features arranged along each border of an implanted area. The features show a dark-bright contrast along the field direction which is inverted after field reversal. Since the MFM tip detects only the out-of-plane force component, the contrast is due to

magnetic stray fields from domain boundaries. The MFM images suggest that either (1) the magnetic domains are so small that the lateral change of the stray field occurs on much smaller distances than the lateral resolution of the MFM or (2) the implanted carbon is distributed inhomogeneously. In the latter case, the ferromagnetic phase is nucleated at the border between the carbon-rich and carbon-devoid Mn–Si phase during implantation at 450 °C. An accumulation of carbon at the interface between carbon-rich $Mn_5Si_3C_{1.5}$ and a Si substrate was also inferred from Auger depth profiling [13].

In conclusion, ferromagnetic $Mn_5Si_3C_{0.8}$ films with Curie temperatures well above room temperature have been obtained by $^{12}C^+$-ion implantation. Patterning of initially carbon-free films by ion implantation allows the synthesis of magnetic structures comprised of different magnetic phases. This work suggests a promising way to obtain lateral magnetic hybrid structures in the micrometer and submicrometer range.

6. Miniature Masks for *in-situ* Transport Measurements

We developed a simple experimental set-up that allows the fabrication of submicrometer-spaced planar contacts on a well-defined surface prepared in UHV by metal deposition through a nanostructured silicon-nitride stencil mask [B1.4:1]. Macroscopic contact pads are created by a second metal-deposition step through a Cu stripe mask and are connected *in situ* by means of a spring-loaded carrier. The key concept to fabricate such contacts is the design of two modular carriers. Both the contact and mask carriers were mounted on a carrier base plate, which fulfills the requirements for device manipulation of the UHV system. First, a mask carrier was loaded with a Cu net normally used for transmission electron microscopy, containing a 35-μm wide parallel stripe across a ring with an inner diameter of ≈1.5 mm. This Cu net mask was used to define the spacing between the large contact pads for the leads. The first deposition step defines two macroscopic half circles separated by ~ 30 μm, in which the UHV-prepared sample surface remains unaltered. Thereafter, the mask was exchanged with a nano-structured stencil mask for use as a second shadow mask. The stencil mask consists of a 200-nm thick low-stress $Si_{3+x}N_{4-x}$ membrane which is freely suspended over a 500 μm × 500 μm window in a 200 μm thick Si(100) wafer. The membrane was nanopatterned by focused ion beam (FIB) etching with 30-keV Ga^+ ions. Figure 6 shows scanning electron microscope (SEM) images of the patterned $Si_{3+x}N_{4-x}$ membrane. The FIB-fabricated stencil mask was attached to a second mask carrier and the mask carriers were exchanged. In order to achieve a good alignment, the magnets on the mask carrier can be adjusted *ex situ* using an optical microscope prior to sample introduction.

In the second evaporation step, the metal is deposited onto the sample through the stencil mask. Figure 7 shows SEM images of the final contact configuration after the two-step deposition process. Figure 7(b) demonstrates that contacts with a separation of d = 700 nm can be easily produced. Each contact has a shallow halo of ≈ 130 nm due to enhanced emission of secondary electrons in the vicinity of the metal structure. The irregular edge is presumably due to the half-shadow h arising from the finite width b of the evaporation source. Using $h \approx 130$ nm we obtain $d_2 \approx 13$ μm as an upper limit of the mask-sample distance during evaporation. This shows that the mask can indeed be positioned at such small distances to the sample using our mask carriers. Finally, the contact carrier was attached to the sample holder generating an electrical contact between the contact pads on the sample surface and a contact on the sample holder which serves as a contact pad itself for a spring attached to our STM. Each of the four springs is connected individually to a pin of an electrical feedthrough in the STM. After attaching the contact carrier, electrical contact between a pair of springs and a macroscopic pad, respectively, is achieved. By measuring the resistances

between the pair of contacts on a same pad, we could establish that indeed stable electrical contacts had been made to the sample surface.

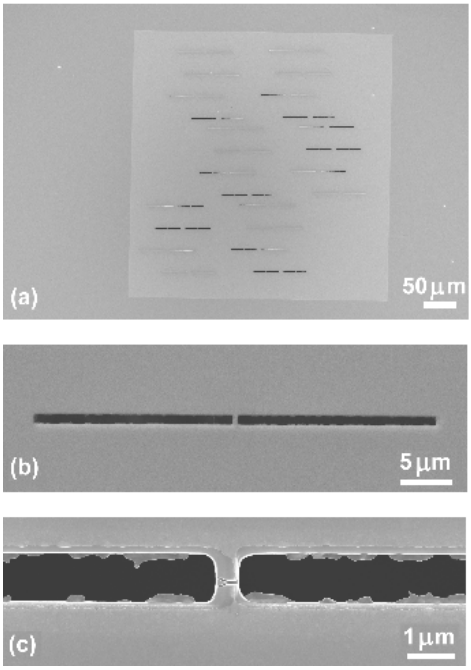

Fig. 6: SEM images of a FIB patterned $Si_{3+x}N_{4-x}$ membrane.

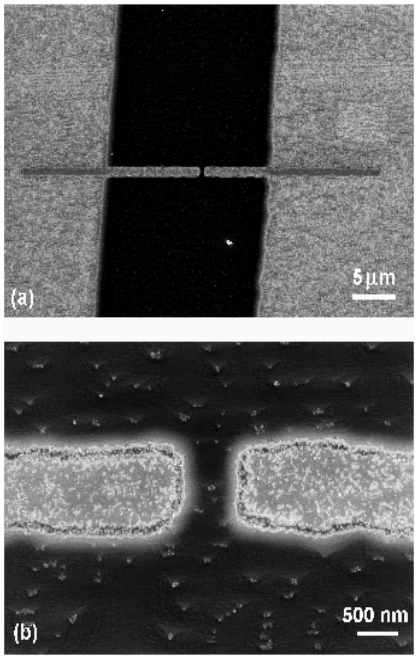

Fig. 7: SEM images of submicrometer-spaced contacts obtained by two-step deposition of Pd through the Cu mask and the nanostructured stencil mask. The unmetallized sample surface appears dark.

In conclusion, planar electrical contacts with submicrometer spacing can be obtained by a two-step process based on a macroscopic mask (Cu), and a nanostructured stencil mask. Stencil masks with a high aspect ratio can be obtained by FIB after stabilizing the $Si_{3+x}N_{4-x}$ membrane by metallization of both sides. The contacts are obtained by metal deposition through the masks in close distance with the substrate. The method is purely mechanical, resistless, and UHV compatible.

7. Fabrication of Nanocontacts by Controlled Electromigration

The electronic transport through metallic contacts and wires can be studied down to the single-atom level [14]. Recently it has been shown that electromigration can be used to form electrodes with nanogaps for molecular junctions [15]. A nanowire or nanocontact is heated resistively until thermally activated atoms diffuse under the influence of electromigration forces. Thinning by electromigration works well when the series resistance of the leads is minimized or when a cycling process, intended to limit the power dissipated in the junction, is used [15,16]. We have recently shown that the latter method yields reproducible results even when nanowires with considerable resistances are used [B1.4:7].

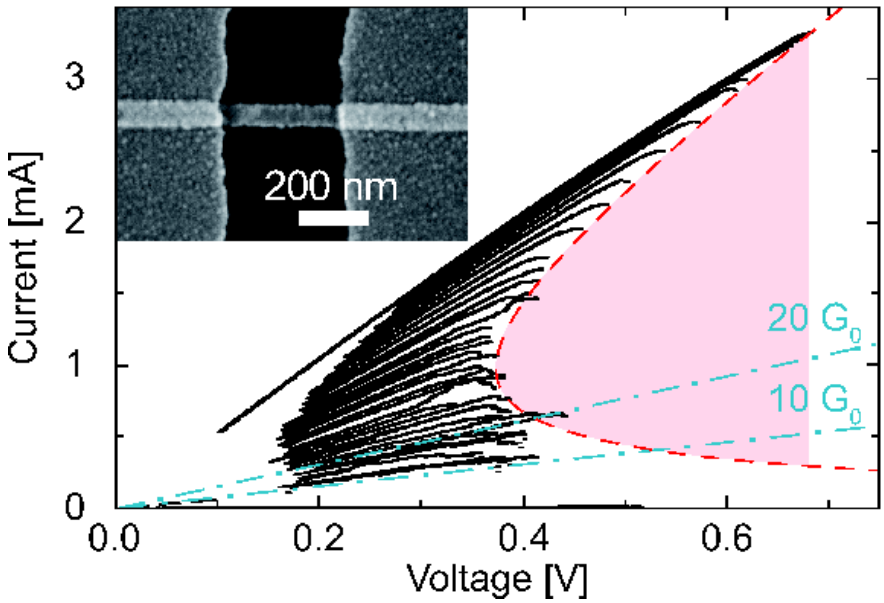

Fig. 8: Current as a function of total voltage U during the electromigration procedure (black data-point traces). The dashed red line shows a constant-power curve with P = 0.18 mW and a lead resistance of R_L = 188 Ω. Dash-dotted blue lines correspond to conductances of 10 and 20 G_0. Inset: SEM image of a nanowire.

Nanowires were prepared by electron-beam lithography in two steps: First, 20-nm thick gold nanowires were prepared on a Si(001) substrate covered by native oxide. Then, large contact pads consisting of a 2-nm thick Cr layer and a 30-nm thick Au layer were evaporated. Scanning electron microscopy (SEM) images show that the gold nanowires are between 300 and 330 nm long, between 60 and 150 nm wide. The nanowires are considered as a network of interconnected grains, in agreement with the overall large resistances between 90 and 950 Ω. The nanowires used in our work seemingly appear unaltered in SEM images after finishing the electromigration measurements. This indicates that gaps smaller than about 10 to 20 nm have been produced in agreement with recent transmission electron microscopy results. For the thinning process, a dc voltage was applied in a cyclic fashion. For each cycle, the voltage was automatically increased in steps of 1 mV per

100 ms until an overall resistance increase $\alpha = \Delta R/ R_0$ between 1 and 6 % of the initially measured resistance R_0 was detected. The voltage was then automatically reduced such that the power was reduced to 20 % of the maximal power reached in this cycle and then the next cycle was started.

We model the device during the thinning process as a nanocontact with variable contact resistance R_C in series with a constant lead resistance R_L, with a total applied voltage

$$U = U_C + U_L = P_C/I + R_L I \quad (1)$$

where U_C and U_L are the voltages across the contact and the leads, respectively, and I is the current. The contact resistance R_C is assumed to be zero at the start of the process and increases during thinning. Obviously, it is not desirable to work at constant current, because when R_C increases, the voltage and thus the power dissipated at the contact would increase during thinning. When one works at constant total voltage, on the other hand, the power dissipated at the contact increases during thinning as well. We have observed that nanowires melt when a sufficiently large voltage is applied. It was therefore our aim to define a process that limits the power dissipated in the contact. The "dangerous" region between a line of a given constant voltage and an allowed constant-power contour with appropriate parameters for our setup is indicated by the shaded region in Fig. 8.

Therefore the cycling process has been designed in order to limit the power dissipated at the contact, assuming that the resistance change α depends monotonically on the temperature of the junction attained by Joule heating and therefore corresponds to a certain heating power. Fig. 8 shows a constant-power curve (Eq. 1) in an *I-V* plot (dashed line). For three samples, indeed, the maximal values reached in each electromigration cycle follow closely a curve of constant power (Fig. 8). However, when the total resistance R exceeds values that correspond to 10 to 20 conductance quanta $G_0 = 2e^2/h$, the pre-chosen value of α is reached for smaller voltages and hence smaller power than expected. One reason that the resistance change is reached at lower dissipated power during the last stages of thinning may be that the actual contact is disconnected from the substrate surface, and is therefore less efficiently cooled. Likewise for two samples with initial resistances of 390 and 950 Ω, the power is not constant during the thinning process. However, in these cases the experimental procedure leads to a controlled increase of the contact resistance as well.

References

- own work with complete titles -

[1] R. Losio, K. N. Altmann, A. Kirakosian, J.-L. Lin, D. Y. Petrovykh, and F. J. Himpsel, Phys. Rev. Lett. **86**, 4632 (2001)
[2] J. R. Ahn, H. W. Yeom, H. S. Yoon, and I.-W. Lyo, Phys. Rev. Lett. **91**, 196403 (2003)
[3] D. Sánchez-Portal, S. Riikonen, and R. M. Martin, Phys. Rev. Lett. **93**, 146803 (2004)
[4] M. Krawiec, T. Kwapiński, and M. Jałochowski, Phys. Rev. B **73**, 075415 (2006)
[5] J. Li, W.-D. Schneider, R. Berndt, O. R. Bryant, S. Crampin, Phys. Rev. Lett. **81**, 4464 (1998)
[6] G. Neuhold and K. Horn, Phys. Rev. Lett. **78**, 1327 (1997)
[7] N. Agrait, A. Levy Yeyati, J.M. van Ruitenbeek, Phys. Rep. **377**, 81 (2003)
[8] R. Q. Wu, G. W. Peng, L. Liu, Y. P. Feng, Z. G. Huang, and Q. Y. Wu, Appl. Phys. Lett. **89**, 062505 (2006)
[9] A. L. Rosa and R. Ahuja, Appl. Phys. Lett. **91,** 232109 (2007)

[10] J.-H. Lee, I.-H. Choi, S. Shin, S. Lee, J. Lee, C. Whang, S.-C.Lee, K.-R. Lee, J.-H. Baek, K. H. Chae, J. Song, Appl. Phys. Lett. **90**, 032504 (2007)
[11] J. Hong, J. Appl. Phys. **103**, 063907 (2008)
[12] C. Zeng, S. C. Erwin, L. C. Feldman, A. P. Li, R. Jin, Y. Song, J. R. Thompson, H. H. Weitering, Appl. Phys. Lett. **83**, 5002 (2003)
[13] C. Sürgers, M. Gajdzik, G. Fischer, H. v. Löhneysen, E. Welter, K. Attenkofer *Preparation and structural characterization of ferromagnetic $Mn_5Si_3C_x$ films*, Phys. Rev. B **68**, 174423 (2003)
[14] J. Park et al., Nature **417**, 722 (2002), H. Park et al., Appl. Phys. Lett. **75**, 301 (1999)
[15] D. R. Strachan, D. E. Smith, D. E. Johnston, T.-H. Park and M. J. Therien, Appl. Phys. Lett. **86**, 043109 (2005)
[16] G. Esen and M. S. Fuhrer, Appl. Phys. Lett. **87**, 263101 (2005)